Computers in Biology and Medicine 108 (2019) 31–41

Contents lists available at ScienceDirect

Computers in Biology and Medicine

journal homepage: www.elsevier.com/locate/compbiomed

Design of porous titanium scaffold for complete mandibular reconstruction: The influence of pore architecture parameters

Abir Dutta[a], Kaushik Mukherjee[b,d], Santanu Dhara[c], Sanjay Gupta[d,*]

[a] Advanced Technology Development Centre, Indian Institute of Technology Kharagpur, Kharagpur, 721 302, West Bengal, India
[b] Department of Bioengineering, Imperial College London, South Kensington, SW7 2AZ, UK
[c] School of Medical Science and Technology, Indian Institute of Technology Kharagpur, Kharagpur, 721 302, West Bengal, India
[d] Department of Mechanical Engineering, Indian Institute of Technology Kharagpur, Kharagpur, 721 302, West Bengal, India

ARTICLE INFO

Keywords:
Mandible
Complete mandibular construct
Homogenization technique
Multiscale
Finite element analysis
Stress analysis

ABSTRACT

Patients having a medical history of oral cancer, infectious diseases or trauma are often advised surgical intervention with customized complete mandibular constructs (CMC) made of Titanium (Ti) scaffolds. A numerical framework based on a homogenization technique was developed to investigate the influence of pore architecture parameters on homogenized orthotropic material properties of the scaffolds. A comparative 3D Finite Element (FE) analysis of six CMC models, having homogenized orthotropic material properties, under a mastication cycle, was undertaken to pre-clinically determine the optimal CMC for a patient. Orthotropic material properties of Ti-scaffolds decreased with an increase in the inter-strut distance. Stress and strain distributions of CMC models during right molar bite were investigated. Despite small differences in stress distributions in the 'body' region of CMC models, the overall stress distribution (tensile and compressive) of CMC models (30–32 MPa) were well comparable to that of an intact mandible (34.54 MPa). Higher magnitudes of tensile strains were observed for models with 0.2 mm (9884με) and 0.4 mm strut diameter (SD), both having 0.5 mm inter-strut distance (ID), at articular condyle area, body and symphysis equivalent part of the constructs. The maximum principal tensile strains were higher in the CMC models with 0.5 mm ID as compared to those having 0.3 mm ID. Comparatively, the scaffolds with lesser ID (0.3 mm) resulted in higher stiffness, thereby evoking less principal strains in the CMC models. Moreover, considering the weight of the scaffolds, the CMC models having 0.3 mm ID with 0.2 mm SD and 0.5 mm ID with 0.6 mm SD seemed most appropriate for a patient.

1. Introduction

The increasing rate of critical maxillofacial diseases, such as oral cancer and osteonecrosis [1,2], has induced a steep increase in surgical intervention, using customized mandibular implants. In the majority of the cases, patients are diagnosed at an advanced stage of oral cancer, osteonecrosis of the jaw, and different stages of tumours in the mandible [3]. The patients are advised to undergo partial or full mandibulectomy, according to the severity of the condition [4]. Autologous bone grafts, harvested from the fibula, the radius of the arm, or the iliac crest of pelvic bone of a patient, are commonly used to retain the function and shape of the jawline of a patient undergoing partial mandibulectomy [5]. Despite several advantages of these autografts, donor site morbidity, intra-oral complications, fistula, failure of the grafts are notable disadvantages, which might compel the patient to undergo repeated surgeries [6].

Patients having a medical history of oral cancer, radiation therapy, bisphosphonate medications owing to the development of tumours and teeth extraction, infectious diseases, and trauma are considered to be critical and are often advised surgical intervention with customized mandibular implants. Total mandibulectomy [7–10] is advised and performed in these cases where the host bone is too weak to undergo partial or marginal mandibulectomy. The full mandible of a patient is replaced by a patient-specific metallic complete mandibular construct (CMC) in total mandibulectomy. Among various Titanium alloys, Ti6Al4V is popularly used for CMC, because of its low specific weight and excellent biocompatibility [5,11]. The primary focus of the CMC is to retain the function of the jaw and to maintain aesthetics.

Porous architectures are popularly used to manufacture several bone grafts and implants of Ti-alloys, which enhance bone ingrowth and also reduce the weight. In this regard, Hollister [12] reported that pore dimensions varying between 200 μm and 1200 μm were found to

---

* Corresponding author.
E-mail address: sangupta@mech.iitkgp.ernet.in (S. Gupta).

https://doi.org/10.1016/j.compbiomed.2019.03.004
Received 3 October 2018; Received in revised form 5 March 2019; Accepted 5 March 2019

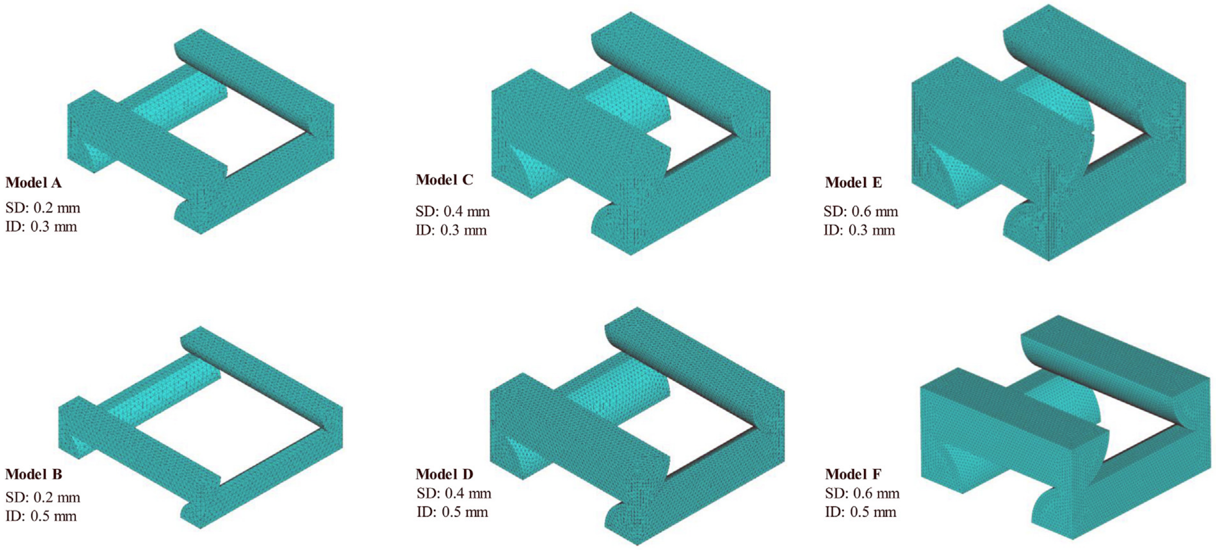

Fig. 1. Specifications of the microscale FE models of the 0°/90° scaffolds. SD: Strut diameter, ID: Inter-strut distance.

be optimum for tissue generation. There are several reports based on detailed characterization of the additively manufactured porous structures having dodecahedron, icosahedron, cubic, rhombohedral and other various shapes of unit cells [13–17]. A numerical homogenization technique, using Finite Element Analysis (FEA), was used to evaluate the effective material properties of scaffolds [18–22]. It was reported by Hollister et al. [18] that the numerical homogenization technique is capable of accurately evaluating the effective material properties of scaffolds. Specifically, Bawolin et al. [19,20] reported that the predicted values from numerical homogenization technique using FEA, for 0°/90° PCL (Polycaprolactone) and HAP (Hydroxyapatite) scaffolds, agreed with the experimental values of compression tests. The values of elastic properties of circular and square cross-section fibre composite materials, predicted using a numerical homogenization technique, were reported to be very close to those calculated using analytical equations [21]. More recently, Roberge et al. [22] used a homogenization technique to predict the elastic properties of the 0°/90° HAP scaffolds. These reports provided confidence in evaluating the effective material properties of 0°/90° Ti-scaffolds using the homogenization technique.

To the author's knowledge, there is hardly any investigation regarding the design criteria of a CMC, built with unit cells of 0°/90° strut orientation having different inter-strut distances. The compressive strength of the 0°/90° scaffolds was reported to be higher than other strut orientations, like 45°/45° [13,23,24]. Higher mechanical strength was reported for 0°/90° oriented PEEK (Polyether-ether-ketone) scaffolds as compared to other strut orientations [23]. Another study by Li et al. [13] reported that additively manufactured Ti-scaffolds having 0°/90° strut orientation, for bone tissue replacement, showed maximum compressive strength in all three directions. Moreover, a recent investigation by Souness et al. [24], observed maximum compressive strength for the 0°/90° structures of PLA (Poly(lactide)) as compared to other strut orientations. These reports provided confidence in the selection of 0°/90° scaffold for further investigation. A notable case study by Xilloc (Xilloc Medical, The Netherlands) is the only available literature, which discussed the design of a CMC weighing 107 g that successfully retained the function of the jaw of an 83-year old female patient [25].

The goal of the study is to develop a numerical framework for the design of a novel patient-specific CMC with 0°/90° circular struts of Ti6Al4V alloy, having different pore architecture parameters. This study is aimed at determining the appropriate set of scaffold parameters for a CMC, having load transfer characteristics closest to an intact mandible. Presumably, notable deviations in load transfer within the construct may result in adverse reaction forces in the temporomandibular joint. The specific objectives are: (1) to develop a numerical framework to obtain the homogenized orthotropic material properties of Ti-scaffolds, and (2) to investigate the load transfer across a CMC with homogenized material properties of the scaffolds subject to a complete mastication cycle.

2. Materials and methods

The numerical framework comprises of microscale three-dimensional (3D) FE models of Ti-scaffolds and macroscale models of the CMC subject to appropriate loading and boundary conditions. The scheme employed a numerical homogenization technique, using Finite Element Analysis (FEA), to predict the elastic orthotropic material coefficients of the scaffolds. In the next phase of the study, 3D FE models of the CMC were simulated with the homogenized orthotropic material properties of the scaffolds to investigate the load transfer during a complete mastication cycle. A comparison of load transfer with an intact mandible was also undertaken.

2.1. Numerical homogenization technique for scaffolds: microscale FE models

The scaffold is generally considered as a macroscale structure. The macroscopic properties of 3D scaffolds were modelled by constructing a representative volume element (RVE) or a unit cell that possessed the features of the microscale structure. The precise modelling and simulation of macroscale scaffolds are generally computationally expensive. The most convenient technique, to facilitate the modelling process of these type of structures and their inherent microscale structures, seemed to be the homogenization technique [26–29]. The central concept of this method is to seek a globally homogeneous continuum equivalent to the original scaffold, where the stored strain energy within the two is approximately equal to each other. The symmetric Ti-scaffolds with 0°/90° orientation between the circular struts of two consecutive layers can be analysed using the RVE approach or a unit cell only (Fig. 1). A unit cell is defined as the smallest part of a scaffold, which contains all the required data of the geometric and material properties of a scaffold at the microscale level, that can be used to deduce the effective properties of the scaffold. Scaffolds are represented as a periodical array of the RVEs. Therefore, the applied boundary conditions on the RVEs must be periodic to conform to the principles of homogenization theory [28]. This corresponds to the fact that there is

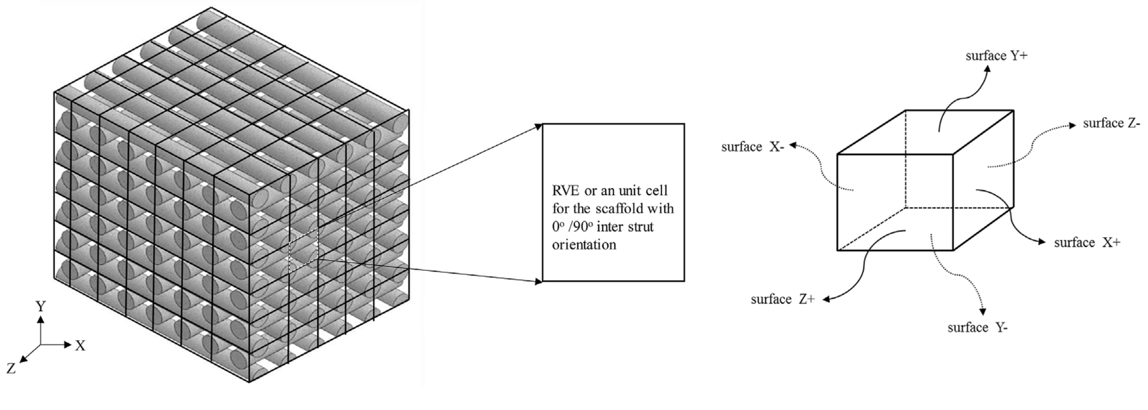

(a) (b)

Fig. 2. Schematic diagram of a periodic scaffold with 0°/90° inter-strut orientation (a) a representative volume element (RVE), (b) boundary surfaces of an RVE cell.

no gap or imbrication between two consecutive RVEs, and each of the RVEs is under the same deformation mode of the macroscale structure. The periodic boundary conditions at the boundary surfaces of the RVE is explained by the following generalised equation [28–30],

$$u_i = \bar{\varepsilon}_{ij} x_j + v_i \tag{1}$$

where $\bar{\varepsilon}_{ij}$ are the average strains, v_i is the periodic part of the displacement components on the boundary surfaces of the RVE, which is unknown, and depends on the applied global loading conditions. The indices i and j denote the global 3D coordinate directions. A more detailed expression for the periodic boundary conditions, appropriate for the RVE models, was derived from the generalised Equation (1). The displacements on two opposite boundary surfaces (e.g., X+ and X-surfaces, Fig. 2) of the RVE are expressed as,

$$u_i^{X+} = \bar{\varepsilon}_{ij} x_j^{X+} + v_i^{X+} \tag{2}$$

$$u_i^{X-} = \bar{\varepsilon}_{ij} x_j^{X-} + v_i^{X-} \tag{3}$$

where the index X+ implies the positive normal direction along x_j direction, and X-implies the negative direction along x_j, corresponding to the opposite two boundary surfaces, X+ and X-, respectively. The local differences between the displacement fields of the two opposite surfaces were exactly similar, owing to the prescribed periodic boundary conditions of the RVE. Hence, the difference between the two displacement fields of the two opposite boundary surfaces was identified as the applied strain condition to the actual macroscopic scaffolds, which is expressed as,

$$u_i^{X+} - u_i^{X-} = \bar{\varepsilon}_{ij} \left(x_j^{X+} - x_j^{X-}\right) \tag{4}$$

The average mechanical properties of RVE were assumed to be the same for those of the scaffolds. The average stresses and strains in an RVE are defined as,

$$\bar{\sigma}_{ij} = \frac{1}{V} \int_V \sigma_{ij} \, dV \tag{5}$$

$$\bar{\varepsilon}_{ij} = \frac{1}{V} \int_V \varepsilon_{ij} \, dV \tag{6}$$

where σ_{ij} is the calculated elemental stress, $\bar{\sigma}_{ij}$ is the average developed stress, calculated by integrating over the RVE volume, V. Similarly, $\bar{\varepsilon}_{ij}$ is the average strain developed in the RVE, calculated by integrating the strain of each element, ε_{ij} over the RVE volume, V.

The FE models of the RVE unit cells of the scaffolds were developed using SOLIDWORKS (SolidWorks, Dassault Systemes S.A.), and meshed in ANSYS FE v15.0 software (Ansys Inc., Canonsburg, PA), using ten-node tetrahedral element [31]. Majority of the early computational models' used 2D beam elements or Timoshenko beam elements for the analysis [14,32]. In comparison, the present study used SOLID187 (ten-node tetrahedral) elements to mesh the struts of the scaffolds, resulting in a more detailed evaluation of the stresses and strains generated in the scaffold unit cells. The element edge length varied between 20 and 40 μm, with a relatively fine mesh at the junction of the two struts. The linear elastic properties of orthotropic materials are defined by the following constitutive relationship,

$$\begin{bmatrix} \bar{\sigma}_{xx} \\ \bar{\sigma}_{yy} \\ \bar{\sigma}_{zz} \\ \bar{\sigma}_{yz} \\ \bar{\sigma}_{zx} \\ \bar{\sigma}_{xy} \end{bmatrix} = \begin{bmatrix} C_{11}^{eff} & C_{12}^{eff} & C_{13}^{eff} & 0 & 0 & 0 \\ C_{21}^{eff} & C_{22}^{eff} & C_{23}^{eff} & 0 & 0 & 0 \\ C_{31}^{eff} & C_{32}^{eff} & C_{33}^{eff} & 0 & 0 & 0 \\ 0 & 0 & 0 & C_{44}^{eff} & 0 & 0 \\ 0 & 0 & 0 & 0 & C_{55}^{eff} & 0 \\ 0 & 0 & 0 & 0 & 0 & C_{66}^{eff} \end{bmatrix} \begin{bmatrix} \bar{\varepsilon}_{xx} \\ \bar{\varepsilon}_{yy} \\ \bar{\varepsilon}_{zz} \\ \bar{\varepsilon}_{yz} \\ \bar{\varepsilon}_{zx} \\ \bar{\varepsilon}_{xy} \end{bmatrix} \tag{7}$$

where $\bar{\sigma}$, $\bar{\varepsilon}$, and C^{eff} are average stress, average strain and components of the effective stiffness matrix for the homogenized orthotropic

Table 1
Prescribed boundary conditions on the opposite surfaces of representative volume element (RVE) corresponding to different load cases for numerical homogenization technique using FE (see Fig. 2).

Load case	Boundary surface					
	X+	X-	Y+	Y-	Z+	Z-
1	*D* along X- direction	constrained along X direction	*PBC*		*PBC*	
2	*PBC*		*D* along Y- direction	constrained along Y direction	*PBC*	
3	*PBC*		*PBC*		*D* along Z- direction	constrained along Z direction
4	*D* along Y+ direction	*D* along Y- direction	*D* along X+ direction	*D* along X- direction	*PBC*	
5	*PBC*		*D* along Z+ direction	*D* along Z- direction	*D* along Y+ direction	*D* along Y- direction
6	*D* along Z+ direction	*D* along Z- direction	*PBC*		*D* along X+ direction	*D* along X- direction

D: Displacement prescribed.
PBC: Periodic boundary conditions prescribed.

scaffolds. The boundary conditions, presented in Table 1, were prescribed for the RVE by coupling the opposite nodes located on the opposite surfaces. Six sets of boundary conditions were imposed in order to obtain the components of the stiffness matrix, which was further used to calculate the orthotropic material properties of the scaffolds, consisting of nine elastic constants (three Young's modulus: E_x, E_y, E_z; three shear modulus: G_{xy}, G_{yz}, G_{xz}; three major Poisson's ratios: ϑ_{xy}, ϑ_{yz}, ϑ_{xz}).

The boundary conditions for each of the load cases of microscale models were prescribed so that, for a particular load case, only the strains in one direction would be non-zero, whereas in all other directions, would be zero. In the case of load case 1, the displacements were prescribed on the nodes of the X+ surface, and the X-surface nodes were restrained from moving along the X-direction. The nodes on the surfaces Y+ and Y- were also restrained from moving along the Y-direction. Similarly, the nodes along the surfaces Z+ and Z-were restrained from moving along the Z-direction. Hence, only the strains developed along the X-direction (ε_{xx}) were non-zero, whereas the strains in all other directions were zero. The resulting average stresses and strains ($\bar{\sigma}$ and $\bar{\varepsilon}$) for each load case were calculated using equations (5) and (6). The corresponding effective coefficient was calculated using non-zero strains and stresses developed based on the constitutive equation for orthotropic materials (Equation (7)). A summary of the method used to determine the elastic coefficients of orthotropic material properties of the scaffolds is presented in Fig. 3.

The RVE size is considered to be a key factor in obtaining reliable results using numerical homogenization technique. A sensitivity study revealed that for 0°/90° Ti-scaffolds, having a regular geometrical pattern, the results are not sensitive to the size of the RVE. The findings of this study led to the choice of the single unit cell as RVE of the scaffolds.

2.2. Design parameters of scaffolds

The strut diameter (SD) and inter-strut distance (ID) were considered as two design parameters and were strategized, based on available literature [12,13,33,34]. This part of the study was focussed on investigating the influence of SD and ID on the homogeneous orthotropic material coefficients of the scaffolds. Isotropic material properties of Ti-alloy (Ti6Al4V), Young's modulus 110 GPa, and Poisson's ratio 0.3 were assigned to all RVEs of the scaffolds.

2.3. Macroscale FE models of intact and complete mandibular constructs

The FE model of an intact mandible was based on a CT-scan dataset of a 35-year old female patient, stored in 512 × 512 pixels, with a pixel size of 0.383 mm, slice thickness of 6 mm [35]. The mandible was segmented into cortical and cancellous bone volumes using image processing software MIMICS v10.0 (Materialise, Leuven, Belgium). Ten-node tetrahedral elements were used to mesh the solid model in ANSYS v15.0. The element edge length varied between 0.5 mm and 1.5 mm. The FE model consisted of 270216 elements and 386159 nodes [35]. The cortical layer of the mandible was subdivided into five distinct

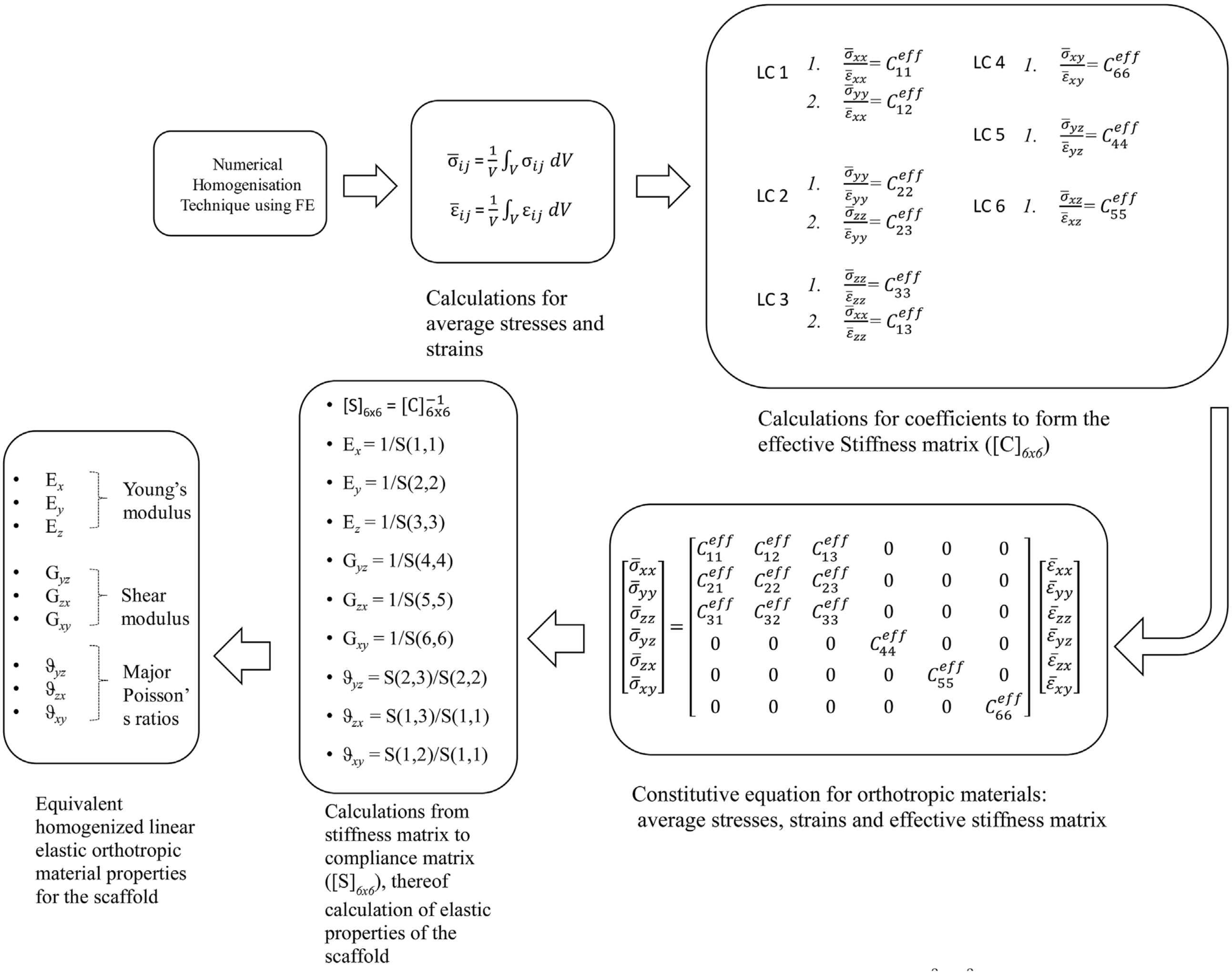

Fig. 3. A schematic representation for the calculation of homogenized orthotropic material properties of the 0°/90° scaffolds.

regions (symphysis, body, ramus, condyle, and coronoid), which, were assigned orthotropic material properties [36–38]. The cancellous bone material properties were assumed to be heterogeneous and isotropic. The elastic modulus of each bone element was calculated from the CT-scan data using Bonemat v2.0 [39]. The apparent density (ρ in g.cm^{-3}) for the bone element was incorporated from the corresponding CT number (HU) in Hounsfield Unit using the relationship,

$$\rho = \rho_1 + [(\rho_2 - \rho_1)/(\mathrm{HU}_2 - \mathrm{HU}_1)]\times[\mathrm{HU} - \mathrm{HU}_1] \tag{8}$$

where (ρ_1, HU_1) represented the apparent density and CT number of water, i.e., no bone condition (0.022 g cm^{-3}, 0 HU), and (ρ_2, HU_2) was the apparent density in the hardest cortical region and corresponding CT number value (1.73 g cm^{-3}, 2600 HU), respectively. Any negative CT grey value was flushed to 0 HU, representing no bone condition [40–42]. The Young's modulus of the mandibular cancellous bone was determined using the modulus-density relationship, $E = 2017.3\ \rho^{2.46}$ [43]. This particular relationship predicted the average Young's modulus of 850 MPa for the cancellous bone, which was close to 960 MPa reported earlier for mandible [44]. Poisson's ratio was assumed to be 0.3 [45,46]. The macroscale FE models of CMC were based on the same CT-scan dataset and the same mesh of the intact mandible (Fig. 4). The CMC models were assigned orthotropic material properties of the homogenized scaffolds, based on the method described in Sec. 2.1.

The FE models of an intact mandible and the CMCs were subjected to a complete mastication cycle. The mastication cycle was divided into six load cases, i.e., incisive, intercuspal position, right molar bite, left molar bite, right group function and left group function. Each of the macroscale CMC models included seven muscle forces as follows: superficial masseter (SM), deep masseter (DM), medial pterygoid (MP), inferior lateral pterygoid (ILP), anterior temporalis (AT), middle temporalis (MT) and posterior temporalis (PT). The magnitudes and directions of the musculoskeletal forces, corresponding to six static load cases of the complete mastication cycle, applied for the macroscale models were based on Korioth et al. [44,47]. The masticatory muscle forces were applied as loading conditions and were uniformly distributed on the patched areas of the FE models of the intact mandible and CMCs [48–50]. The highest amount of stresses and strains in the mandible were observed for the right molar bite. For this load case, the nodes located on the occlusal surface of the Right Molar teeth, were constrained along the transverse axis of the mandible, and the articular condyles were restrained from moving along the two orthogonal directions of the transverse axes. The details of the muscle forces and boundary conditions, during a complete mastication cycle, are presented in Table 2 [47,51].

2.4. Validation and verification of the FE models

A mesh convergence study was performed by comparing the results of three FE models of intact mandible consisting of 113768, 270216, and 787418 numbers of elements. Comparison between the first and second FE models revealed 7% deviations of maximum principal strains in the mandible. However, the range of the deviation was reduced to 4% when the results of the second and third models were compared. The model consisting of 270216 elements, with mesh size varying between 0.5 mm and 1.5 mm, was chosen for the FE model of the intact mandible after comparison between the maximum values of principal tensile strains of three models. Similarly, a separate mesh convergence study for the microscale scaffold models revealed the optimum mesh size varying between 0.02 mm and 0.04 mm. The total number of elements and nodes corresponding to six microscale FE models are presented in Table 3.

The methodology for numerical homogenization technique, using FEA, was validated with the experimental results of Bawolin et al. [19,20]. Direct one-to-one experimental validation of the FE model of the intact mandible was not possible, since the CT-scan dataset was based on a living patient. However, the generation procedure of the FE model of the intact mandible was validated by comparing with the principal stresses and strains at comparable locations (Fig. 5), reported by Korioth et al. [44], using similar loading and boundary conditions. The FE model of Korioth et al. [44] reported high principal tensile stresses varying between 15 and 25 MPa, around the biting area of the right molar teeth. Although the predicted results of our study were qualitatively comparable to those predicted by Korioth et al. [44], differences in the maximum principal stress values (Our model: 34.54 MPa versus 25 MPa of Korioth et al.) were observed at comparable locations for both the models [35,44]. The overall agreement, however, provided confidence in the FE models for further investigations on load transfer across the CMC models. Distribution of principal stresses and strains along with the weight of the CMC were evaluated for the choice of suitable CMC for a patient [52–54].

3. Results

The maximum and minimum values of principal stresses and strains were developed in CMC models during right molar bite (load case 3; Table 2), hence chosen for a detailed analysis. Principal strain distributions in the CMC models were analysed to investigate the influence of scaffold parameters on load transfer across the constructs. Maximum principal strains were recorded as the 99th percentile values to avoid potential stress concentrations at the constrained locations of the models. The generated peak strains were compared with the maximum

(a) (b)

Fig. 4. Finite element model of (a) CMC; (b) showing locations of muscle (M.) attachment sites and boundary conditions (for details see Table 2).
(1) M. Masseter, (2) M. Temporalis, (3) M. Lateral pterygoid, (4) M. Medial pterygoid, (5) Articular condyle (boundary conditions), (6) Molar, (7) Premolar, (8) Canine, (9) Incisor.

Table 2
Muscle forces: SM superficial masseter, DM deep masseter, MP medial pterygoid, ILP inferior lateral pterygoid, AT anterior temporalis, MT middle temporalis, PT posterior temporalis [47,51].

Clenching tasks: INC incisal clench, ICP intercuspal position, RMOL right unilateral molar clench, LMOL left unilateral molar clench, RGF right group function, LGF left group function.

Clenching tasks	Side	Direction	Muscular force (N)							Boundary Condition
			SM	DM	MP	AT	MT	PT	ILP	
INC	Right	Force	76.2	21.2	136.4	12.6	5.7	3.0	47.5	Constrained the incisor regions
		F_x	−15.8	−11.6	66.3	−1.9	−1.3	−0.6	29.9	
		F_y	67.3	16.1	107.8	12.5	4.8	1.4	−8.3	
		F_z	31.9	−7.6	50.9	0.6	−2.9	−2.6	36.0	
	Left	Force	76.2	21.2	136.4	12.6	5.7	3.0	47.5	
		F_x	15.8	11.6	−66.3	1.9	1.3	0.6	−29.9	
		F_y	67.3	16.1	107.8	12.5	4.8	1.4	−8.3	
		F_z	31.9	−7.6	50.9	0.6	−2.9	−2.6	36.0	
ICP	Right	Force	190.4	81.6	132.9	154.9	91.8	71.0	18.1	Constrained the canine and premolars
		F_x	−39.4	−44.6	64.6	−23.1	−20.4	−14.8	11.4	
		F_y	168.3	61.9	105.1	153.0	76.8	33.7	−3.1	
		F_z	79.80	−29.2	49.61	6.8	−45.9	−60.8	13.7	
	Left	Force	190.4	81.6	132.9	154.9	91.8	71.0	18.1	
		F_x	39.4	44.6	−64.6	23.1	20.4	14.8	−11.4	
		F_y	168.3	61.9	105.1	153.0	76.8	33.7	−3.1	
		F_z	79.8	−29.2	49.6	6.8	−45.9	−60.8	13.7	
RMOL	Right	Force	137.1	58.8	146.9	115.4	63.1	44.6	20.1	Constrained the right molars
		F_x	−28.4	−32.1	71.4	−17.2	−14.0	−9.3	12.6	
		F_y	121.2	44.5	116.1	114.0	52.8	21.1	−3.5	
		F_z	57.4	−21.0	54.8	5.1	−31.5	−38.1	15.2	
	Left	Force	114.2	49.0	104.9	91.7	64.0	29.5	43.5	
		F_x	23.6	26.7	−51.0	13.7	14.2	6.1	−27.4	
		F_y	101.0	37.1	83.0	90.5	53.6	14.0	−7.6	
		F_z	47.9	−17.5	39.1	4.0	−32.0	−25.2	32.9	
LMOL	Right	Force	114.2	49.0	104.9	91.7	64.0	29.5	43.5	Constrained the left molars
		F_x	−23.6	−26.7	51.0	−13.7	−14.2	−6.1	27.4	
		F_y	101.0	37.1	83.0	90.5	53.6	14.0	−7.6	
		F_z	47.9	−17.5	39.1	4.0	−32.0	−25.2	32.9	
	Left	Force	137.1	58.8	146.9	115.4	63.1	44.6	20.1	
		F_x	28.4	32.1	−71.4	17.2	14.0	9.3	−12.6	
		F_y	121.2	44.5	116.1	114.0	52.8	21.1	−3.5	
		F_z	57.4	−21.0	54.8	5.1	−31.5	−38.1	15.2	
RGF	Right	Force	34.3	29.4	12.2	104.3	61.2	46.8	39.5	Constrained the right canine, premolars and molars
		F_x	−7.1	−16.0	5.9	−15.5	−13.6	−9.7	24.9	
		F_y	45.4	16.1	105.1	10.9	4.8	2.2	−1.6	
		F_z	21.5	−7.6	49.6	0.5	−2.9	−3.9	7.1	
	Left	Force	51.4	21.2	132.9	11.1	5.7	4.5	9.4	
		F_x	10.6	11.6	−64.6	1.6	1.3	0.9	−5.9	
		F_y	45.4	16.1	105.1	10.9	4.8	2.2	−1.6	
		F_z	21.5	−7.6	49.6	0.5	−2.9	−3.9	7.1	
LGF	Right	Force	51.4	21.2	132.9	11.1	5.7	4.5	9.4	Constrained the left canine, premolars and molars
		F_x	−10.6	−11.6	64.6	−1.6	−1.3	−0.9	5.9	
		F_y	45.4	16.1	105.1	10.9	4.8	2.2	−1.6	
		F_z	21.5	−7.6	49.6	0.5	−2.9	−3.9	7.1	
	Left	Force	34.3	29.4	12.2	104.3	61.2	46.8	39.5	
		F_x	7.1	16.0	−5.9	15.5	13.6	9.7	−24.9	
		F_y	45.4	16.1	105.1	10.9	4.8	2.2	−1.6	
		F_z	21.5	−7.6	49.6	0.5	−2.9	−3.9	7.1	

Table 3
The total number of elements and nodes corresponding to six microscale FE models.

Microscale Models		
Model	Elements	Nodes
A	2040	3970
B	19713	32297
C	85796	127082
D	106420	157644
E	245649	351994
F	297936	425893

strain generated in an intact mandible to identify appropriate scaffold pore architecture parameters for the CMC. In the next step, the weights of the selected CMCs were compared with the weight of the intact mandible to identify the preferred sets of scaffold parameters that may be suitable for additive manufacturing. The effective density of the Ti-scaffolds and the volume of the mandible were calculated, thereof the weight of the CMC models was evaluated.

The design parameters of the 0°/90° scaffolds were found to have considerable influence on the predicted homogenized orthotropic material coefficients. The values of Young's modulus (E) and shear modulus (G) were observed to increase with an increase in SD (Table 4). The values of E and G, however, were found to decrease with an increase in

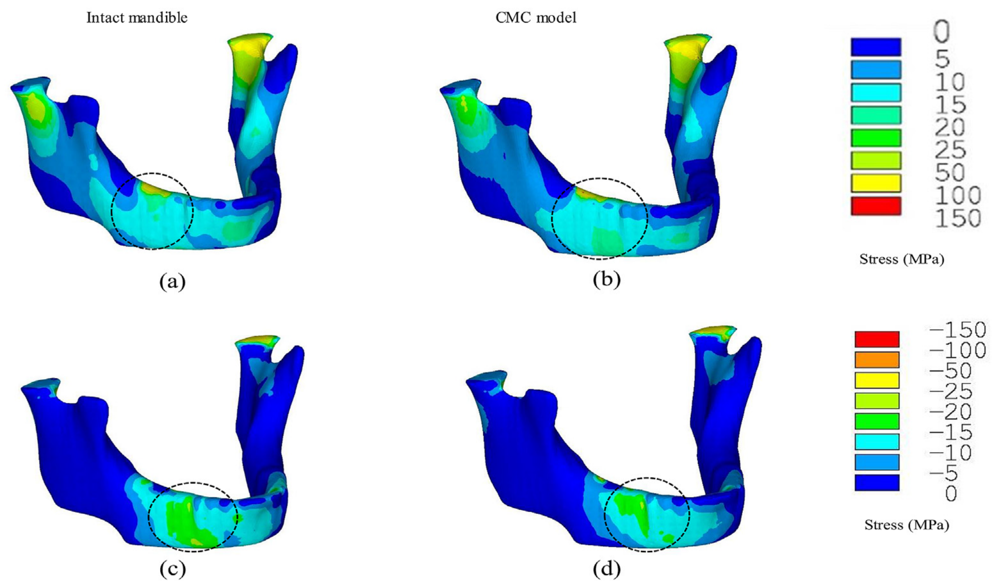

Fig. 5. Principal tensile and compressive stress (MPa) distributions in a representative CMC model compared to an intact mandible corresponding to unilateral right molar clenching (load case 3); (a) intact mandible-principal tensile stress, (b) CMC model-principal tensile stress, (c) intact mandible-principal compressive stress, (d) CMC model-principal compressive stress. High stress regions are encircled.

the ID from 0.3 mm to 0.5 mm (Table 4). The maximum values of orthotropic material properties were obtained for the scaffold having the highest strut diameter (SD = 0.6 mm) and the lowest inter-strut distance (ID = 0.3 mm), whereas minimum values were obtained for the scaffold having the lowest strut diameter (SD = 0.2 mm) and the highest inter-strut distance (ID = 0.5 mm). Predicted values of major Poisson's ratio are presented in Table 4.

The stresses and strains in the intact mandible were observed to be maximum in the case of right molar bite (load case 3). The maximum principal stress of 34.54 MPa, was generated in the intact mandible. The maximum principal strain was found to be 3267 με. Overall, the stress distributions corresponding to load case 3 for the intact mandible (Fig. 5a,c) was found to be well comparable with those reported by Korioth et al. [44]. The distributions of principal stresses and strains for all the CMC models (with each of the six sets of orthotropic material properties) were obtained for six load cases of a complete mastication cycle. The stresses and strains were found to be maximum during right molar bite (load case 3). The overall principal tensile and compressive stress distributions for all the CMC FE models were found to be very similar as compared to the intact mandible. Hence one representative set of tensile and compressive stress distributions is presented in Fig. 5. Results indicated that there were small differences in stress distribution at the 'body' region of the CMC models. However, the overall stress distribution (tensile and compressive) in the CMC models (30–32 MPa) were found to be very well compared with those of an intact mandible (34.54 MPa). The distributions of principal strains (tensile) in the six CMC FE models for load case 3 are shown in Fig. 6. Higher magnitudes of tensile strains were observed for Model 'B' and 'D' at articular condyle area, body and symphysis equivalent part of the constructs. The maximum principal tensile strains were observed to be higher in the CMC models with 0.5 mm ID as compared to those having 0.3 mm ID (Fig. 7). An increase in maximum principal strains was observed with a reduction in the SD, since it led to the reduction of the effective elastic moduli of homogenized scaffolds. A maximum principal tensile strain of 9884 με was observed for the CMC with homogenized material properties of the scaffolds with 0.2 mm SD and 0.5 mm ID.

The weight of the CMC with six set of scaffold parameters was also evaluated and presented in Fig. 8. The weight of the CMC, closest to the intact mandible, was found to be 98.17 g, having the scaffold architecture parameters of 0.2 mm SD with 0.3 mm ID. The lowest weight, recorded for the CMC having scaffold parameters of 0.2 mm SD with 0.5 mm ID, was 72 g. The heaviest CMC was found to be of 168.4 g with scaffold architecture parameters of 0.6 mm SD and 0.3 mm ID.

4. Discussion

In this study, a numerical homogenization framework using FEA has been employed to investigate the influence of pore architecture parameters on the homogenized orthotropic material properties of Ti-scaffolds. The novelty of the study lies in comparative 3D FE analysis of CMCs, having homogenized effective orthotropic material properties, and subject to a complete mastication cycle, in order to pre-clinically determine the most appropriate CMC for a patient. Overall, the study is an attempt to identify potential scaffold architecture parameters, which might lead to an optimal CMC, thus reducing chances of revision surgeries and construct failure. Results indicated a considerable influence of the pore architecture parameters on the homogenized orthotropic material properties of the scaffolds. The scaffolds with 0.2 mm SD

Table 4
Homogenized linear elastic orthotropic material properties of the scaffolds. For specifications of Models A – F, see Fig. 1.

Model	Homogenized linear elastic material properties								
	Young's modulus (GPa)			Shear modulus (GPa)			Major Poisson's ratios		
	E_x	E_y	E_z	G_{yz}	G_{zx}	G_{xy}	ϑ_{yz}	ϑ_{zx}	ϑ_{xy}
A	17.92	7.63	18.79	2.67	0.78	2.39	0.16	0.009	0.15
B	13.72	4.10	13.08	1.29	0.45	1.28	0.15	0.008	0.16
C	24.93	10.87	26.87	2.90	0.73	2.55	0.16	0.005	0.15
D	21.96	7.27	20.36	1.64	0.47	1.87	0.15	0.004	0.16
E	31.18	12.66	31.98	3.36	1.23	3.38	0.16	0.010	0.15
F	26.71	11.52	23.61	2.92	0.88	3.62	0.15	0.006	0.16

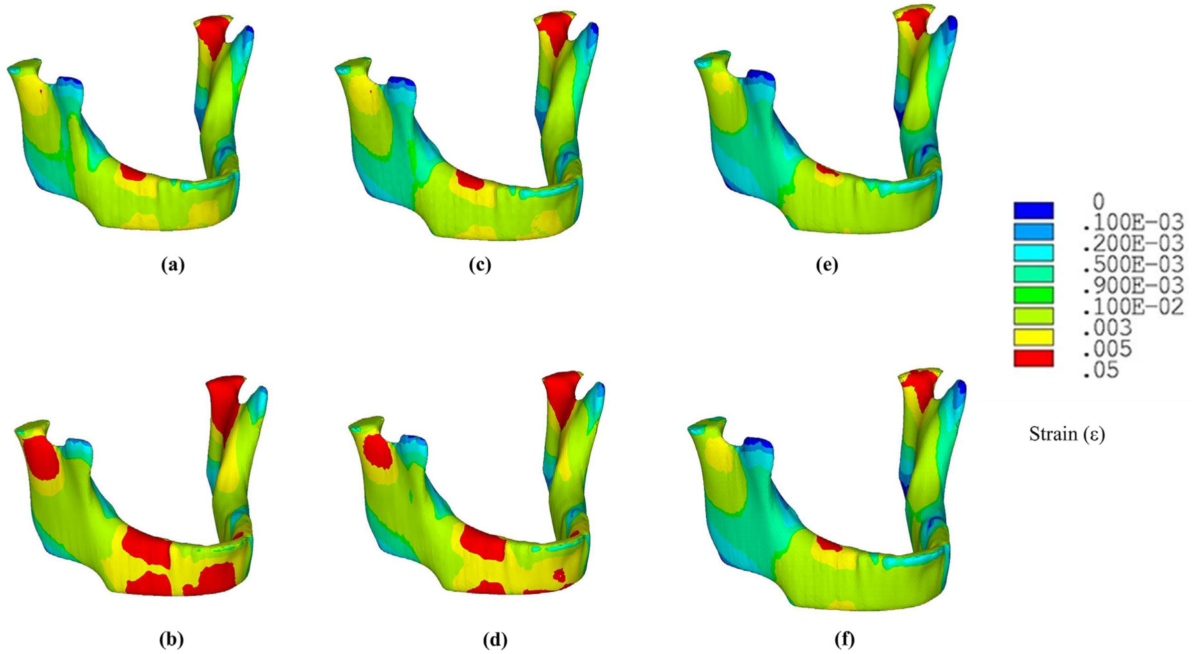

Fig. 6. Principal tensile strain (ε) distribution for CMC models (isometric view) for unilateral right molar clenching (load case 3): (a) Model A, (b) Model B, (c) Model C, (d) Model D, (e) Model E, and (f) Model F.

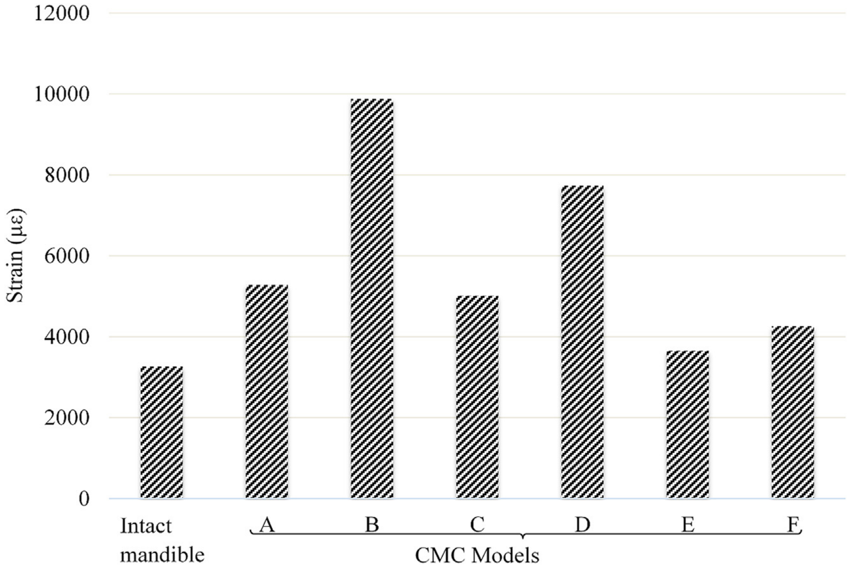

Fig. 7. Comparison of the maximum principal tensile strains in the intact mandible and the CMC models during right molar bite (load case 3).

yielded elastic coefficients values less than those of the intact mandible. The elastic modulus values were found to increase with an increase in the SD. The models with 0.4 mm SD, having both 0.3 mm and 0.5 mm ID, were found to have elastic modulus values close to the intact mandible [36–38]. Moreover, the scaffolds with 0.6 mm SD, having an ID of 0.3 mm, was found to be slightly higher (11.35%) than the elastic coefficients reported for the intact mandible. The homogenized orthotropic material properties were observed to decrease with an increase in the ID; Young's modulus of the Ti-scaffolds, having 0.37 mm SD, was reported to decrease with an increase in the ID [13]. These corroborations with earlier studies served as a qualitative validation, providing confidence in the numerically predicted results.

The principal stress distributions of the CMC models were observed to be less sensitive to variations in homogenized material properties of the scaffolds. However, notable differences were observed amongst the principal strain distributions of the CMC models. It was observed that Model ‘E’ and ‘F’ exhibited principal strain distributions very similar to the intact mandible owing to the similarity between the material properties of the two scaffolds and the intact mandible. The maximum principal strain developed in an intact mandible during load case 3 was 3267 με [35], and weight of the same was noted to be 98 g, which is also supported by Zhang et al. [55].

Based on the comparison of maximum principal strains and the overall strain distributions of the CMC models to those of the intact mandible, Model ‘E’ and ‘F’ appeared to be the most appropriate. However, the weight of the CMC is an important parameter from the viewpoint of the patient. In this regard, Model ‘B’ seemed to be the CMC with the lowest weight of 72 g, but having very high principal strains (9884 με) around the body and symphysis area. Whereas, Model ‘A’ (maximum principal strain for the right molar bite: 5278 με) and Model

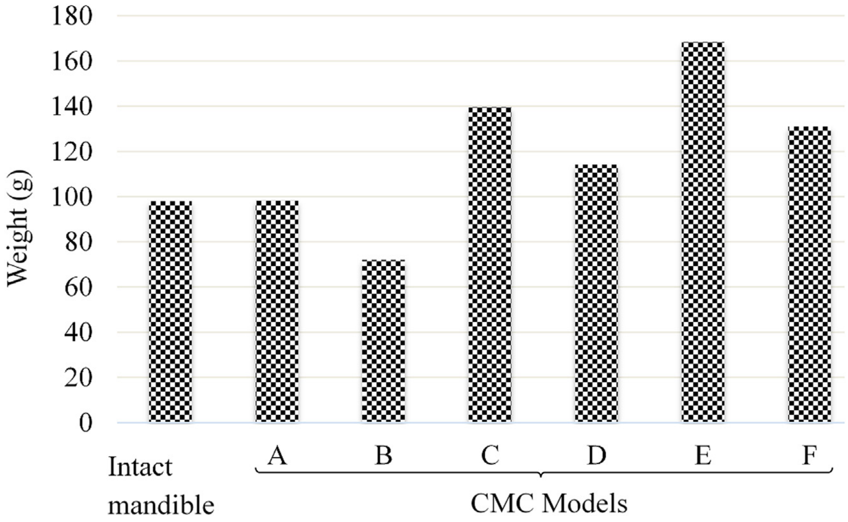

Fig. 8. Comparison of weights: CMC models and intact mandible.

'F' (maximum principal strain for the right molar bite: 4263 με), appeared to be better models, weighing 98.17 g and 131.05 g, respectively.

The current study, however, has some limitations. It has been reported that irregularities and micro-level discontinuities within the struts of the scaffolds, after manufacturing, plays a key role in determining the values of its effective elastic coefficients. Moreover, it is also reported that the effective material properties of scaffolds are considerably influenced by the manufacturing processes. The effects on the material properties of a scaffold, owing to the manufacturing processes, have not been investigated in this study. Moreover, the surface morphology (roughness and presence of micropores) of the manufactured CMC requires further investigation for host response within the oral environment. The linear elastic CMC models were simulated under one complete mastication cycle. The experimental characterization of the additively manufactured implants, under the chewing forces, has not been investigated. The CT-scan dataset was based on a single patient. Hence, inter-patient variability has not been considered in this study. The results, therefore, are patient specific and should be interpreted within the limitations of this study. This study, however, presented a novel multiscale framework for determining homogenized material properties of 0°/90° Ti-scaffolds and thereby, investigated the influence of scaffold architecture parameters on the design of CMC.

Based on the results of this study, it appeared that a reduction in the SD and an increase in the ID caused a reduction in the homogenized orthotropic material properties of the scaffolds. However, a simultaneous increase in the SD and the ID resulted in homogenized orthotropic material properties similar to those of an intact mandible. Scaffolds with lesser ID (0.3 mm) resulted in higher stiffness, thereby evoking less principal strains in the CMC models, during the right molar bite. Moreover, considering the weight of scaffolds, the model A (0.3 mm ID with 0.2 mm SD) and the model F (0.5 mm ID with 0.6 mm SD), seemed to be most appropriate for a patient.

5. Conclusions

Based on this study, the following conclusions may be drawn:

(1) The effective homogenized orthotropic material properties of scaffolds were influenced by strut diameter and inter-strut distance. The effective material properties of the scaffold with 0.6 mm strut diameter having 0.3 inter-strut distance, were found to be similar to the material properties of an intact mandible.
(2) Strut diameter and inter-strut distance had a negligible effect on the principal stress distributions of the CMC models but had considerable influence on the principal tensile strain distribution.
(3) For 0°/90° strut orientation, scaffold architecture, with 0.2 mm SD having 0.3 mm ID and 0.6 mm SD having 0.5 mm ID, seemed to be most appropriate for the design of Ti-CMC.

Author contributions statements

Abir Dutta and Kaushik Mukherjee wrote the main manuscript. Sanjay Gupta and Santanu Dhara supervised the research. All authors reviewed the manuscript.

Conflict of interest

We, hereby, state that with regard to the submission of this research paper there is no financial and personal relationships with other people and organizations.

Acknowledgement

The authors wish to thank Indian Institute of Technology Kharagpur, India for supporting this study.

Appendix A. Supplementary data

Supplementary data to this article can be found online at https://doi.org/10.1016/j.compbiomed.2019.03.004.

References

[1] R.E. Marx, Pamidronate (Aredia) and Zoledronate (Zometa) induced avascular necrosis of jaws: a growing epidemic, J. Oral Maxillofac. Surg. 61 (9) (2003) 1115 https://doi.org/org/10.1016/S0278-2391(03)00720-1.
[2] J. Ferlay, I. Soerjomataram, R. Dikshit, S. Eser, C. Mathers, M. Rebelo, D.M. Parkin, D. Forman, F. Bray, IARC Cancer Base No. 11, GLOBOCAN 2012 v1.0, Cancer Incidence and Mortality Worldwide vol. 10, International Agency for Research on Cancer, Lyon, France, 2013.
[3] Z. Cai, C. Zhu, L. Wang, L. Zhu, Z. Zhang, H. Zhu, Y. Wang, A retrospective study of six patients with mandibular metastatic carcinoma, Oncol. Lett. 11 (6) (2016) 3650–3654, https://doi.org/10.3892/ol.2016.4484.
[4] S.M. Park, J.W. Lee, G. Noh, Which plate results in better stability after segmental mandibular resection and fibula free flap reconstruction? Biomechanical analysis, Oral Surg. Oral Med. Oral Pathol. Oral Radiol. 126 (5) (2018) 380–389, https://doi.org/10.1016/j.oooo.2018.05.048.
[5] N. Narra, J. Valášek, M. Hannula, P. Marcián, G.K. Sándor, J. Hyttinen, J. Wolff, Finite element analysis of customized reconstruction plates for mandibular continuity defect therapy, J. Biomech. 47 (1) (2014) 264–268, https://doi.org/10.1016/j.jbiomech.2013.11.016.
[6] C. Rendenbach, A. Rashad, L. Hansen, C. Kohlmeier, M.L. Dyck, A. Suling,

A.T. Assaf, M. Amling, M. Heiland, J. Wikner, B. Riecke, K. Kreutzer, Functional donor site morbidity longer than one year after fibula free flap: a prospective biomechanical analysis, Microsurgery 38 (4) (2018) 395–401, https://doi.org/10.1002/micr.30205.

[7] M. Motlagh, M. Bayat, S. Naji, Bone allograft: an option for total mandibular reconstruction, Craniomaxillofacial Trauma Reconstr. 10 (04) (2017) 306–313, https://doi.org/10.1055/s-0036-1593474.

[8] D.B. Rodrigues, L.M. Wolford, P. Malaquias, P.S.F. Campos, Concomitant treatment of mandibular ameloblastoma and bilateral temporomandibular joint osteoarthritis with bone graft and total joint prostheses, J. Oral Maxillofac. Surg. 73 (1) (2015) 63–74, https://doi.org/10.1016/j.joms.2014.06.461.

[9] C.A.R. Valero, G. Duran-Rodriguez, N. Solano-Parra, J. Castro-Núñez, Immediate total temporomandibular joint replacement with tmj concepts prosthesis as an alternative for ameloblastoma cases, J. Oral Maxillofac. Surg. 72 (3) (2014) 646, https://doi.org/10.1016/j.joms.2013.09.026 e1.

[10] D. Grinsell, B.Y.T. Yue, S.I. Ferris, Total mandibular reconstruction using four free flap transfers in a patient with large mandibular osteosarcoma, Eur. J. Plast. Surg. 37 (10) (2014) 563–566, https://doi.org/10.1007/s00238-014-0990-0.

[11] J. Chaurand, L. Pacheco-Ruíz, Bilateral total mandibular reconstruction with patient specific implants for temporomandibular joint ankylosis, J. Stomatol. Oral Maxillofac. Surg. 119 (4) (2018) 354–356, https://doi.org/10.1016/j.jormas.2018.05.003.

[12] S.J. Hollister, Porous scaffold design for tissue engineering, Nat. Mater. 4 (7) (2005) 518–524, https://doi.org/10.1093/jb/mvj031.

[13] J.P. Li, J.R. De Wijn, C.A. Van Blitterswijk, K. De Groot, The effect of scaffold architecture on properties of direct 3D fiber deposition of porous Ti6Al4V for orthopedic implants, J. Biomed. Mater. Res. A 92 (1) (2010) 33–42, https://doi.org/10.1002/jbm.a.32330.

[14] G. Campoli, M.S. Borleffs, S. Amin Yavari, R. Wauthle, H. Weinans, A.A. Zadpoor, Mechanical properties of open-cell metallic biomaterials manufactured using additive manufacturing, Mater. Des. 49 (2013) 957–965, https://doi.org/10.1016/j.matdes.2013.01.071.

[15] S. Amin Yavari, R. Wauthle, J. van der Stok, A.C. Riemslag, M. Janssen, M. Mulier, J.P. Kruth, J. Schrooten, H. Weinans, A.A. Zadpoor, Fatigue behavior of porous biomaterials manufactured using selective laser melting, Mater. Sci. Eng. C 33 (8) (2013) 4849–4858, https://doi.org/10.1016/j.msec.2013.08.006.

[16] S.M. Ahmadi, G. Campoli, S. Amin Yavari, B. Sajadi, R. Wauthle, J. Schrooten, H. Weinans, A.A. Zadpoor, Mechanical behavior of regular open-cell porous biomaterials made of diamond lattice unit cells, J. Mech. Behav. Biomed. Mater. 34 (2014) 106–115, https://doi.org/10.1016/j.jmbbm.2014.02.003.

[17] S.M. Ahmadi, S.A. Yavari, R. Wauthle, B. Pouran, J. Schrooten, H. Weinans, A.A. Zadpoor, Additively manufactured open-cell porous biomaterials made from six different space-filling unit cells: the mechanical and morphological properties, Materials (Basel) 8 (4) (2015) 1871–1896, https://doi.org/10.3390/ma8041871.

[18] S.J. Hollister, D.P. Fyhrie, K.J. Jepsen, S.A. Goldstein, Application of homogenization theory to the study of trabecular bone mechanics, J. Biomech. 24 (9) (1991) 825–839, https://doi.org/10.1016/0021-9290(91)90308-A.

[19] N.K. Bawolin, Modeling material-degradation-induced elastic property of tissue engineering scaffolds, J. Biomech. Eng. 132 (11) (2010) 111001, https://doi.org/10.1002/elan.201200153.

[20] N.K. Bawolin, X.B. Chen, Remote determination of time-dependent stiffness of surface-degrading-polymer scaffolds via synchrotron-based imaging, J. Biomech. Eng. 139 (4) (2017) 041004, , https://doi.org/10.1115/1.4036021.

[21] S.B.R. Devireddy, S. Biswas, Effect of fiber geometry and representative volume element on elastic and thermal properties of unidirectional fiber-reinforced composites, JEC Compos. 2014 (2014) 1–12, https://doi.org/10.1155/2014/629175.

[22] J. Roberge, J. Norato, Computational design of curvilinear bone scaffolds fabricated via direct ink writing, CAD Comput. Aided Des. 95 (2018) 1–13, https://doi.org/10.1016/j.cad.2017.09.003.

[23] W. Wu, P. Geng, G. Li, D. Zhao, H. Zhang, J. Zhao, Influence of layer thickness and raster angle on the mechanical properties of 3D-printed PEEK and a comparative mechanical study between PEEK and ABS, Materials (Basel) 8 (9) (2015) 5834–5846, https://doi.org/10.3390/ma8095271.

[24] A. Souness, F. Zamboni, G.M. Walker, M.N. Collins, Influence of scaffold design on 3D printed cell constructs, J. Biomed. Mater. Res. B Appl. Biomater. 106 (2) (2018) 533–545, https://doi.org/10.1002/jbm.b.33863.

[25] https://www.xilloc.com/patients/stories/total-mandibular-implant , Accessed date: 27 September 2018.

[26] H. Berger, U. Gabbert, H. Köppe, R. Rodriguez-Ramos, J. Bravo-Castillero, R. Guinovart-Diaz, J.A. Otero, G.A. Maugin, Finite element and asymptotic homogenization methods applied to smart composite materials, Comput. Mech. 33 (1) (2003) 61–67, https://doi.org/10.1007/s00466-003-0500-x.

[27] E. Lenglet, A.-C. Hladky-Hennion, J.-C. Debus, Numerical homogenization techniques applied to piezoelectric composites, J. Acoust. Soc. Am. 113 (2) (2003) 826, https://doi.org/10.1121/1.1537710.

[28] H. Berger, S. Kari, U. Gabbert, R. Rodriguez-Ramos, R. Guinovart, J.A. Otero, J. Bravo-Castillero, An analytical and numerical approach for calculating effective material coefficients of piezoelectric fiber composites, Int. J. Solids Struct. 42 (21–22) (2005) 5692–5714, https://doi.org/10.1016/j.ijsolstr.2005.03.016.

[29] H. Berger, S. Kari, U. Gabbert, R. Rodriguez-Ramos, J. Bravo-Castillero, R. Guinovart-Diaz, F.J. Sabina, G.A. Maugin, Unit cell models of piezoelectric fiber composites for numerical and analytical calculation of effective properties, Smart Mater. Struct. 15 (2) (2006) 451–458, https://doi.org/10.1088/0964-1726/15/2/026.

[30] P. Suquet, Elements of homogenization theory for inelastic solid mechanics, in: E. Sanchez-Palencia, A. Zaoui (Eds.), Homogenization Techniques for Composite Media, Springer-Verlag, Berlin, 1987, pp. 194–275.

[31] M. Viceconti, L. Bellingeri, L. Cristofolini, A. Toni, A comparative study on different methods of automatic mesh generation of human femurs, Med. Eng. Phys. 20 (1) (1998) 1–10, https://doi.org/10.1016/S1350-4533(97)00049-0.

[32] J. Parthasarathy, B. Starly, S. Raman, A. Christensen, Mechanical evaluation of porous titanium (Ti6Al4V) structures with electron beam melting (EBM), J. Mech. Behav. Biomed. Mater. 3 (3) (2010) 249–259, https://doi.org/10.1016/j.jmbbm.2009.10.006.

[33] M. Dallago, V. Fontanari, E. Torresani, M. Leoni, C. Pederzolli, C. Potrich, M. Benedetti, Fatigue and biological properties of Ti-6Al-4V ELI cellular structures with variously arranged cubic cells made by selective laser melting, J. Mech. Behav. Biomed. Mater. 78 (2018) 381–394, https://doi.org/10.1016/j.jmbbm.2017.11.044.

[34] N. Taniguchi, S. Fujibayashi, M. Takemoto, K. Sasaki, B. Otsuki, T. Nakamura, T. Matsushita, T. Kokubo, S. Matsuda, Effect of pore size on bone ingrowth into porous titanium implants fabricated by additive manufacturing: an in vivo experiment, Mater. Sci. Eng. C 59 (2016) 690–701, https://doi.org/10.1016/j.msec.2015.10.069.

[35] A. Dutta, K. Mukherjee, S. Dhara, S. Gupta, A numerical investigation on the influence of location and size of lesion on load transfer in an osteonecrotic mandible, 8th World Congress of Biomechanics, 8-12 July 2018, Dublin, Ireland, 2018, p. P1148.

[36] J. Huo, P. Dérand, L.E. Rännar, J.M. Hirsch, E.K. Gamstedt, Failure location prediction by finite element analysis for an additive manufactured mandible implant, Med. Eng. Phys. 37 (9) (2015) 862–869, https://doi.org/10.1016/j.medengphy.2015.06.001.

[37] S. Lovald, B. Baack, C. Gaball, G. Olson, A. Hoard, Biomechanical optimization of bone plates used in rigid fixation of mandibular symphysis fractures, J. Oral Maxillofac. Surg. 68 (8) (2010) 1833–1841, https://doi.org/10.1016/j.joms.2009.09.108.

[38] C.L. Schwartz-Dabney, P.C. Dechow, Variations in cortical material properties throughout the human dentate mandible, Am. J. Phys. Anthropol. 120 (3) (2003) 252–277, https://doi.org/10.1002/ajpa.10121.

[39] F. Taddei, A. Pancanti, M. Viceconti, An improved method for the automatic mapping of computed tomography numbers onto finite element models, Med. Eng. Phys. 26 (1) (2004) 61–69, https://doi.org/10.1016/S1350-4533(03)00138-3.

[40] K. Mukherjee, S. Gupta, The effects of musculoskeletal loading regimes on numerical evaluations of acetabular component, Proc. Inst. Mech. Eng. Part H J. Eng. Med. 230 (10) (2016) 918–929, https://doi.org/10.1177/0954411916661368.

[41] K. Mukherjee, S. Gupta, Bone ingrowth around porous-coated acetabular implant: a three-dimensional finite element study using mechanoregulatory algorithm, Biomechanics Model. Mechanobiol. 15 (2) (2016) 389–403, https://doi.org/10.1007/s10237-015-0696-7.

[42] K. Mukherjee, S. Gupta, Mechanobiological simulations of peri-acetabular bone ingrowth: a comparative analysis of cell-phenotype specific and phenomenological algorithms, Med. Biol. Eng. Comput. 55 (3) (2017) 449–465, https://doi.org/10.1007/s11517-016-1528-3.

[43] M. Dalstra, R. Huiskes, A. Odgaard, L. van Erning, Mechanical and textural properties of pelvic trabecular bone, J. Biomech. 26 (4–5) (1993) 523–535, https://doi.org/10.1016/0021-9290(93)90014-6.

[44] T.W. Korioth, D.P. Romilly, A.G. Hannam, Three-dimensional finite element stress analysis of the dentate human mandible, Am. J. Phys. Anthropol. 88 (1) (1992) 69–96, https://doi.org/10.1002/ajpa.1330880107.

[45] K. Mukherjee, S. Gupta, Influence of implant surface texture design on peri-acetabular bone ingrowth: a mechanobiology based finite element analysis, J. Biomech. Eng. 139 (3) (2017) 031006, , https://doi.org/10.1115/1.4035369.

[46] K. Mukherjee, S. Gupta, Combined bone ingrowth and remodeling around uncemented acetabular component: a multiscale mechanobiology-based finite element analysis, J. Biomech. Eng. 139 (9) (2017) 091007, , https://doi.org/10.1115/1.4037223.

[47] T.W. Korioth, A.G. Hannam, Mandibular forces during simulated tooth clenching, J. Orofac. Pain 8 (2) (1994) 178–189.

[48] M. Mesnard, A. Mesnard, A. Ramos, V.A. Lokhov, Y.I. Nyashin, Characterization of the muscular and articular forces exerted on the mandible. Experimental and calculative methods, Russian J. Biomech. 19 (2) (2015) 124–136, https://doi.org/10.15593/RJBiomech/2015.2.02.

[49] A. Ramos, H. Marques, M. Mesnard, The effect of mechanical properties of bone in the mandible, a numerical case study, Adv. Biomech. Appl. 1 (1) (2014) 67–76, https://doi.org/10.12989/aba.2013.1.1.067.

[50] A. Ramos, A. Ballu, M. Mesnard, P. Talaia, J.A. Simões, Numerical and experimental models of the mandible, Exp. Mech. 51 (7) (2011) 1053–1059, https://doi.org/10.1007/s11340-010-9403-x.

[51] L. Hijazi, W. Hejazi, M.A. Darwich, K. Darwich, Finite element analysis of stress distribution on the mandible and condylar fracture osteosynthesis during various clenching tasks, Oral Maxillofac. Surg. 20 (4) (2016) 359–367, https://doi.org/10.1007/s10006-016-0573-2.

[52] R. Yan, D. Luo, H. Huang, R. Li, N. Yu, C. Liu, M. Hu, Q. Rong, Electron beam melting in the fabrication of three-dimensional mesh titanium mandibular prosthesis scaffold, Sci. Rep. 8 (1) (2018) 750, https://doi.org/10.1038/s41598-017-15564-6.

[53] A. Ramos, L.M. Gonzalez-Perez, P. Infante-Cossio, M. Mesnard, Ex-vivo and in vitro validation of an innovative mandibular condyle implant concept, J. Cranio-Maxillofacial Surg. 47 (1) (2019) 112–119, https://doi.org/10.1016/j.jcms.2018.11.010.

[54] M. Hirota, T. Shima, I. Sato, T. Ozawa, T. Iwai, A. Ametani, M. Sato, Y. Noishiki, T. Ogawa, T. Hayakawa, I. Tohnai, Development of a biointegrated mandibular

reconstruction device consisting of bone compatible titanium fiber mesh scaffold, Biomaterials 75 (2016) 223–236, https://doi.org/10.1016/j.biomaterials.2015.09.034.

[55] F. Zhang, C.C. Peck, A.G. Hannam, Mass properties on the human mandible, J. Biomech. 35 (7) (2002) 975–978, https://doi.org/10.1016/S0021-9290(02)00057-X.

Mr. Abir Dutta is pursuing Doctoral research in Biomaterials and Biomechanics at Advanced Technology Development Centre, IIT Kharagpur.

Dr. Kaushik Mukherjee,Ph.D. (IIT Kharagpur) is a postdoctoral researcher at Department of Bioengineering, Imperial College London. His research domain is orthopaedic biomechanics and implant design.

Dr. Santanu Dhara, Ph.D. (IIT Kharagpur) has expertise in Biomaterials and Tissue Engineering and is currently a Professor of School of Medical Science and Technology, IIT Kharagpur.

Prof. Sanjay Gupta, Ph.D. (TU Delft) has 20 years of research experience in Orthopaedic Biomechanics and is currently a Professor of Mechanical Engineering, Indian Institute of Technology Kharagpur.